Repulsive nature of optical potentials for high-energy heavy-ion scattering

T. Furumoto*
Yukawa Institute for Theoretical Physics, Kyoto University, Kyoto 606-8502, Japan and
RIKEN Nishina Center, Wako, Saitama 351-0198, Japan

Y. Sakuragi†
Department of Physics, Osaka City University, Osaka 558-8585, Japan and
RIKEN Nishina Center, RIKEN, Wako, Saitama 351-0198, Japan

Y. Yamamoto‡
Physics Section, Tsuru University, Tsuru, Yamanashi 402-8555, Japan
(Received 8 September 2010; published 25 October 2010)

The recent works by the present authors predicted that the real part of heavy-ion optical potentials changes its character from attraction to repulsion around the incident energy per nucleon $E/A = 200$–300 MeV on the basis of the complex G-matrix interaction and the double-folding model (DFM) and revealed that the three-body force plays an important role there. In the present paper, we have precisely analyzed the energy dependence of the calculated DFM potentials and its relation to the elastic-scattering angular distributions in detail in the case of the $^{12}C + ^{12}C$ system in the energy range of $E/A = 100$–400 MeV. The tensor force contributes substantially to the energy dependence of the real part of the DFM potentials and plays an important role to lower the attractive-to-repulsive transition energy. The nearside and farside (N/F) decompositions of the elastic-scattering amplitudes clarify the close relation between the attractive-to-repulsive transition of the potentials and the characteristic evolution of the calculated angular distributions with the increase of the incident energy. Based on the present analysis, we propose experimental measurements for the predicted strong diffraction phenomena of the elastic-scattering angular distribution caused by the N/F interference around the attractive-to-repulsive transition energy together with the reduced diffractions below and above the transition energy.

DOI: 10.1103/PhysRevC.82.044612 PACS number(s): 24.50.+g, 24.10.Ht, 25.70.Bc

I. INTRODUCTION

The self-consistent nuclear mean field for finite-nuclear systems is an attractive potential as a whole, and nucleons in a nucleus are bound in such an attractive single-particle potential. The attractive nature of the nuclear potentials is smoothly connected to the positive-energy region of the nucleon-scattering states [1]. The optical potentials for low-energy nucleons scattered by finite nuclei are known to have an attractive real part together with an absorptive imaginary part. However, the optical potential for nucleons is highly dependent on the incident energy, and the depth of the attractive real part is known to become shallower as the energy increases. The strength of the interior part decreases more rapidly than that of the surface part, leading to the so-called wine-bottle-bottom shape for $E_{in} \geqslant 200$–300 MeV, and finally, the potential changes its sign from negative (attractive) to positive (repulsive), first at the interior part and then at the surface part also around $E_{in} \approx 500$–800 MeV [2–8]. The origin of such a transition of the optical potentials from attractive to repulsive has been discussed microscopically based on nucleon-nucleon interactions both in the relativistic and in the nonrelativistic frameworks.

A similar attractive-to-repulsive transition of optical potentials was found for intermediate-energies deuteron-nucleus scattering [9–12]. The similarity of proton scattering and deuteron scattering is quite natural for high-scattering energies because of the small binding energy of the deuteron. The characteristic feature of deuteron scattering is known to be well understood in the picture of impulse or sudden approximation, in which the deuteron-nucleus-scattering amplitude is written in good approximation as the coherent sum of the proton-nucleus scattering with the neutron as a spectator and the neutron-nucleus scattering with the proton as a spectator [13]. However, no such attractive-to-repulsive transition of optical potentials has been studied theoretically nor proved experimentally for scattering of composite projectiles other than the loosely bound deuteron. The only exception was a report on the possible repulsive optical potentials for intermediate-energy α-nucleus scattering [14], but it was far from conclusive.

Recently, the present authors have proposed a theoretical model for constructing the complex optical potential for any composite projectiles through the double-folding-model (DFM) procedure by using a newly proposed complex G-matrix NN interaction called CEG07 [15–17] and demonstrated that the folding model provides quite reliable complex optical potentials for intermediate-energy scattering of light heavy ions, such as ^{16}O and ^{12}C, by various target nuclei. One of the major findings of this paper is the discovery of the decisive role of the three-body force (TBF) effect (or

*furumoto@yukawa.kyoto-u.ac.jp
†sakuragi@sci.osaka-cu.ac.jp
‡yamamoto@tsuru.ac.jp

that of the three-nucleon correlations in a nuclear medium). The repulsive part of the TBF is found to be of particular importance, which contributes dominantly at the density region higher than the saturation density ρ_0. Because of this repulsive effect, the strength of nucleus-nucleus potential is reduced strongly at short distances where densities of two nuclei overlap with each other [16,17]. The experimental data for elastic scattering of ^{16}O and ^{12}C projectiles by various target nuclei at $E/A = 70$–135 MeV are well reproduced over the whole angular range only when the G-matrix interactions with the TBF effects (CEG07b or CEG07c) are used in constructing the DFM potentials, while the data cannot be reproduced at all with the use of the CEG07a interaction generated from the two-body force only [17]. Since the TBF effect in nuclear matter plays an essential role to make the saturation curve and the incompressibility K reasonable, these results imply that the proper nucleus-nucleus interaction models should be based on a consistent treatment of the properties of infinite-nuclear matter and the optical potentials between interacting finite-nuclear systems.

Another important finding was that the folding model predicted the repulsive optical potential for the incident energy per nucleon of $E/A \approx 400$ MeV [17], and the attractive-to-repulsive transition was found to occur below this energy, say, around $E/A \approx 200$–300 MeV, although not explicitly mentioned in Ref. [17]. These energies are apparently lower than the energies ($E/A \approx 300$–400 MeV) at which the proton and deuteron optical potentials start to change their signs from negative (attractive) to positive (repulsive). To our knowledge, this is the first theoretical prediction of the repulsive nature of optical potentials for heavy-ion scattering based on the microscopic interaction model, which starts from the free-space NN interaction, although no experimental data exist so far on the heavy-ion elastic scattering in this energy range.

In the course of the folding-model analyses of $^{16}\mathrm{O} + {}^{16}\mathrm{O}$ elastic scattering mentioned previously [17], we noticed an interesting sign, which suggested the attractive-to-repulsive transition of the optical potential in the characteristic evolution of angular distribution shapes of the elastic cross sections as the incident energy increases, although it was not explicitly discussed in Ref. [17] either. Figure 1 shows the differential cross sections of the $^{16}\mathrm{O} + {}^{16}\mathrm{O}$ elastic scattering at $E/A =$ 100–400 MeV presented in Ref. [17] calculated with the DFM potential evaluated from the CEG07a (dashed curves) and CEG07b (solid curves) interactions.[1] One may notice that the diffraction pattern of the differential cross section shows a characteristic and drastic change with the increase of the incident energy. Namely, the cross section calculated with CEG07b exhibits a strong diffraction pattern around $E/A \approx 300$ MeV, whereas the oscillation amplitude is very small below and above this energy. (In fact, it is at this energy that the real part of the folding potential changes its character effectively from attractive to repulsive, as shown later in this paper.) This transition energy looks shifted to the higher-energy side by about 100 MeV (i.e., $E/A \approx 400$ MeV) in the case with the CEG07a interaction that gives a less repulsive folding potential than the CEG07b one does at $E/A \approx 400$ MeV, as discussed in Ref. [17]. In addition, one can also see that the cross sections calculated with CEG07a dominate over those calculated with CEG07b below $E/A \approx 300$ MeV, while the situation is completely reversed above this energy, as seen in Fig. 1.

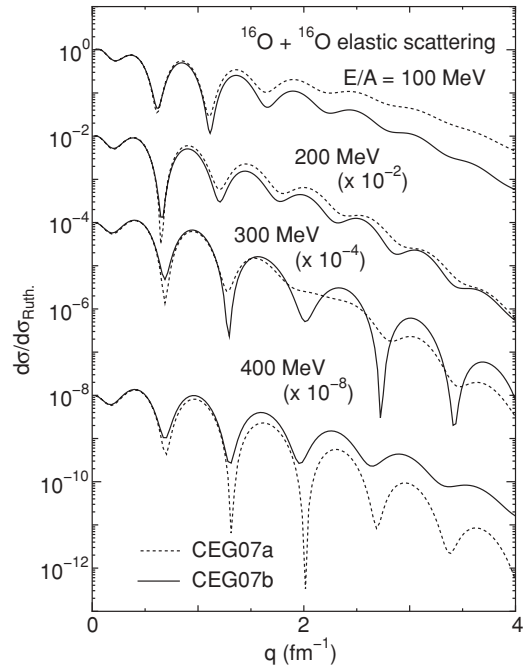

FIG. 1. Rutherford ratio of the differential cross sections for the $^{16}\mathrm{O} + {}^{16}\mathrm{O}$ elastic scattering at $E/A = 100$, 200, 300, and 400 MeV, displayed as the functions of the momentum transfer q. The dotted and solid curves are the results with CEG07a and CEG07b, respectively, with $N_W = 1.0$. This N_W value is defined in Ref. [17] and Sec. II.

The purpose of the present paper is to analyze the characteristic behavior of the elastic-scattering cross sections with the increase of the incident energy in detail in this energy region and to study its close relation to the attractive-to-repulsive transition of the optical potential predicted by the folding model, which will give us an experimental signature for identifying evidence of the attractive-to-repulsive transition of optical potentials for nucleus-nucleus systems. To this end, we decompose the calculated differential cross sections into the nearside and farside (N/F) components [19] to clarify the attractive or repulsive contribution of the optical potential to the differential cross sections. In this paper, we analyze the $^{12}\mathrm{C} + {}^{12}\mathrm{C}$ elastic scattering instead of the $^{16}\mathrm{O} + {}^{16}\mathrm{O}$ one presented in Ref. [17] for the sake of experimental feasibility of measurements and, hence, of the possible comparison of the experimental data with the theoretical predictions.

II. FOLDING-MODEL CALCULATIONS

The CEG07 complex G-matrix interaction is derived from an NN interaction in free space by solving the

[1]There was an error in the calculated G matrices for high energies as noted in Ref. [18], the calculated results shown here in Fig. 1 are corrected from those given in Fig. 16 of Ref. [17] in the cases of CEG07a and CEG07b.

Bethe-Goldstone equation in nuclear matter with the scattering boundary condition. We adopted the latest version of the extended soft-core model (ESC04) [20,21] as the free-space NN interaction. The obtained G-matrix interaction in coordinate space is parametrized with three-range Gaussian form factors for each spin-isospin component, which depends on the nucleon energy and the density of nuclear matter. We proposed the three types of interactions, CEG07a, CEG07b, and CEG07c [15], the latter two, which include the TBF effect in a different manner, as already mentioned in Sec. I. The TBF consists of two components, the attractive TBF and the repulsive TBF [15,17]. The detailed form of the CEG07 interactions and their parameters are given in Ref. [18] for $E/A = 70$–140 MeV and in the Appendix of the present paper for $E/A = 200$, 300, and 400 MeV.

In the present folding model, the complex optical potential for a nucleus-nucleus system is calculated in the DFM with the use of the CEG07 interaction. The direct and exchange parts of the DFM potential are written in the standard form [22,23] as

$$U_{\rm D}(R) = \int \rho_1(\boldsymbol{r}_1)\rho_2(\boldsymbol{r}_2)v_{\rm D}(s;\rho, E/A)\,d\boldsymbol{r}_1\,d\boldsymbol{r}_2, \qquad (1)$$

and

$$U_{\rm EX}(R) = \int \rho_1(\boldsymbol{r}_1, \boldsymbol{r}_1+\boldsymbol{s})\rho_2(\boldsymbol{r}_2, \boldsymbol{r}_2-\boldsymbol{s})v_{\rm EX}(s;\rho, E/A) \times \exp\left[\frac{i\boldsymbol{k}(R)\cdot\boldsymbol{s}}{M}\right] d\boldsymbol{r}_1\,d\boldsymbol{r}_2, \qquad (2)$$

where $\boldsymbol{s} = \boldsymbol{r}_2 - \boldsymbol{r}_1 + \boldsymbol{R}$. The exchange part, which is originally a nonlocal potential, has been localized in the standard way with the plane-wave representation for the NN relative motion [22,23]. Here, $v_{\rm D}$ and $v_{\rm EX}$ are the direct and the exchange parts of the complex G-matrix interaction CEG07 and are written as

$$v_{\rm D,EX} = \pm\tfrac{1}{16}v^{00} + \tfrac{3}{16}v^{01} + \tfrac{3}{16}v^{10} \pm \tfrac{9}{16}v^{11}, \qquad (3)$$

in terms of the spin-isospin component v^{ST} ($S = 0$ or 1 and $T = 0$ or 1) of the CEG07 interaction. The upper and lower parts of the double-sign symbols correspond to the direct (D) and the exchange (EX) parts, respectively.

In Eq. (2), $\boldsymbol{k}(R)$ is the local momentum for the nucleus-nucleus relative motion defined by

$$k^2(R) = \frac{2mM}{\hbar^2}[E_{\rm c.m.} - {\rm Re}\,U(R) - V_{\rm Coul}(R)], \qquad (4)$$

where $M = A_1A_2/(A_1 + A_2)$, $E_{\rm c.m.}$ is the center-of-mass energy, E/A is the incident energy per nucleon, m is the nucleon mass, and $V_{\rm Coul}$ is the Coulomb potential. A_1 and A_2 are the mass numbers of the projectile and target, respectively. The exchange part is calculated self-consistently on the basis of the local-energy approximation through Eq. (4). Here, the Coulomb potential $V_{\rm Coul}$ is also obtained by folding the NN Coulomb potential with the proton-density distributions of the projectile and target nuclei. The density matrix $\rho(\boldsymbol{r}, \boldsymbol{r}')$ is approximated in the same manner as in Ref. [24]:

$$\rho(\boldsymbol{r}, \boldsymbol{r}') = \frac{3}{k_F^{\rm eff}s}j_1\left(k_F^{\rm eff}s\right)\rho\left(\frac{\boldsymbol{r}+\boldsymbol{r}'}{2}\right), \qquad (5)$$

where $k_F^{\rm eff}$ is the effective Fermi momentum [25] defined by

$$k_F^{\rm eff} = \left((3\pi^2\rho)^{2/3} + \frac{5C_s[\nabla\rho]^2}{3\rho^2} + \frac{5\nabla^2\rho}{36\rho}\right)^{1/2}, \qquad (6)$$

where we adopt $C_s = 1/4$ following Ref. [26]. The detailed methods for calculating $U_{\rm D}$ and $U_{\rm EX}$ are the same as those given in Refs. [27] and [28], respectively.

In the present calculations, we employ the so-called frozen-density approximation (FDA) for evaluating the local density. In the FDA, the density-dependent NN interaction is assumed to feel the local density defined as the sum of densities of colliding nuclei evaluated at the midpoint of the interacting nucleon pair:

$$\rho = \rho_1\left(\boldsymbol{r}_1 + \tfrac{1}{2}\boldsymbol{s}\right) + \rho_2\left(\boldsymbol{r}_2 - \tfrac{1}{2}\boldsymbol{s}\right). \qquad (7)$$

Also, the FDA has widely been used in the standard DFM calculations [17,28–31], and it was proved that the FDA was the most appropriate prescription for evaluating the local density in the DFM calculations with realistic complex G-matrix interactions [17].

The imaginary part of the calculated potential is multiplied by a renormalization factor N_W, the value of which is the only free parameter in the present folding model. In the previous analyses [16,17], its values were determined so as to reproduce the experimental data on the elastic-scattering cross sections to be compared with the calculated ones. However, there exist no experimental data to be compared with the calculations in the high-energy region $E/A = 100$–400 MeV we discuss in the present paper, and we fix the N_W value to unity unless otherwise mentioned.

We now apply the DFM with the CEG07 G-matrix interaction to the $^{12}{\rm C} + {}^{12}{\rm C}$ elastic scattering at four incident energies $E/A = 100$, 200, 300, and 400 MeV, and analyze the energy dependence of the calculated DFM potentials and its close relation to the elastic-scattering observables, particularly to the evolution of characteristic diffraction pattern of the differential cross sections as the increase of energy. For the nucleon density of ^{12}C, we adopt the density deduced from the charge density [32] extracted from electron-scattering experiments by unfolding the finite-size effect of the proton charge in the standard way [33]. We perform the calculations with the use of the two types of CEG07 interactions, CEG07a (without the TBF effect) and CEG07b (with the TBF one), in parallel.

Figure 2 shows the angular distributions of the $^{12}{\rm C} + {}^{12}{\rm C}$ elastic-scattering cross sections calculated at the four incident energies. The relativistic-kinematics correction has been made when we solve the Schrödinger equation in all the scattering calculations presented in this paper including that of Fig. 1. The evolution of the angular distribution with the incident energy and the difference between the two types of interactions for this scattering system are very similar to those for the $^{16}{\rm O} + {}^{16}{\rm O}$ system shown in Fig. 1. Namely, the calculated cross section with CEG07a dominates over the cross section with CEG07b at the middle and backward angles at $E/A = 100$ MeV, whereas the two kinds of cross sections show almost identical angular distributions at 200 MeV and, as we go to higher energies,

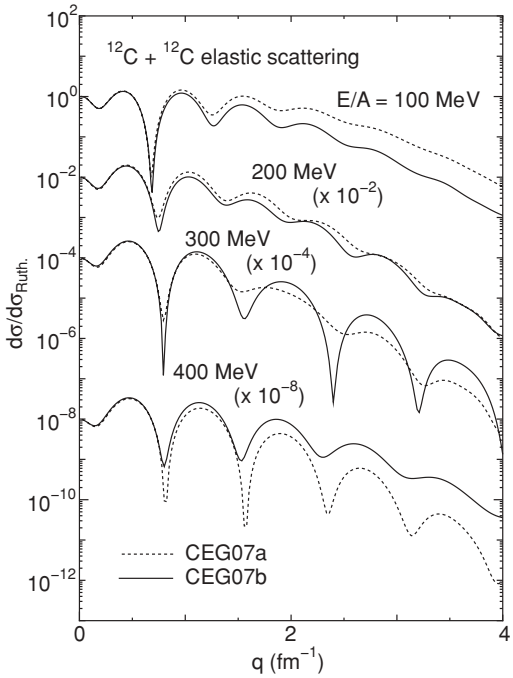

FIG. 2. Same as Fig. 1 but for the $^{12}C + ^{12}C$ system.

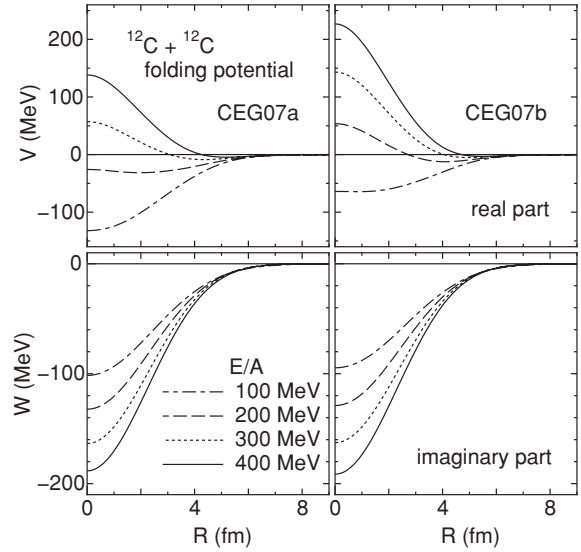

FIG. 3. Real (upper) and imaginary (lower) parts of the DFM potentials calculated with CEG07a (left) and CEG07b (right) for the $^{12}C + ^{12}C$ elastic scattering at $E/A = 100$–400 MeV. The dot-dashed, dashed, dotted, and solid curves are the results at $E/A = 100$, 200, 300, and 400 MeV, respectively.

the latter takes over the former and, at $E/A = 400$ MeV, the situation becomes completely opposite to that of 100 MeV. In addition, the cross sections show a strong diffractive oscillation pattern at 300 MeV for CEG07b and at 400 MeV for CEG07a, respectively, while they show no strong oscillation at other energies.

To investigate the origin of these phenomena, we compare the DFM potentials $U(R) = U_D(R) + U_{EX}(R)$, calculated at the four energies with the CEG07a and CEG07b interactions. Figure 3 shows the real part $[V(R) = \mathrm{Re}\,U(R)]$ and the imaginary part $[W(R) = \mathrm{Im}\,U(R)]$ of the DFM potentials calculated with CEG07a and CEG07b. The imaginary part has a similar shape at all energies for both interactions, and its strength becomes larger as the energy increases, whereas the real part becomes shallower as the energy increases and starts to change its sign from negative (attractive) to positive (repulsive) around $E/A = 300$ MeV for CEG07a and 200 MeV for CEG07b, although it depends on the radial position. It is seen that the DFM potentials with CEG07b are more repulsive by about 80–100 MeV at the origin ($R = 0$) than that with CEG07a at all energies, which is mainly due to the contribution of the repulsive component of the TBF [17].

Here, we should mention the reason why we still use the CEG07a interaction, which has no TBF effect in the present analysis of higher-energy scattering. In the previous papers [16,17], we demonstrated a decisive role of the TBF in properly reproducing the experimental data of elastic scattering at incident energies of $E/A = 70$–135 MeV, and those data could not be reproduced at all by the calculation with CEG07a because of the lack of the TBF effect. However, in the folding model proposed in Refs. [16,17] (and also adopted here), the energy dependence of the TBF has not been considered. In general, various medium effects should disappear in the high-energy limit, and one may naturally expect that the TBF effect, which is one of the medium effects expected to be important in the high-density nuclear medium, will also diminish as the incident energy increases and finally disappears in the high-energy limit. Thus, the TBF effect might become weak at some high-incident energies, although one cannot say at what energy it becomes really negligible within our present modeling for the TBF. Here, we adopt the two extremes, one with no TBF effect represented by CEG07a and the other with a rather strong TBF effect represented by CEG07b, which is nicely valid at least at lower energies $E/A \leqslant 100$ MeV, and test them with the higher-energy scattering. At the moment, we cannot mention which is better at each energy, but the true situation will be in between the two extremes anyway. What is important here is the fact that both interaction models predict strong repulsive potentials around and above $E/A \approx 200$–300 MeV.

Here, we decompose the DFM potential into the spin-isospin components U^{ST}, defined by replacing v_D and v_{EX} in Eqs. (1) and (2) with v^{ST} multiplied by the factor given in Eq. (3). Figure 4 shows the energy dependence of the real part of U^{ST}, $V^{ST} = \mathrm{Re}\,U^{ST}$, in the case of CEG07b. The corresponding figure for CEG07a is not shown here, which is similar to the one for CEG07b except that the potentials given by the former are more attractive than those given by the latter as one can easily imagine from Fig. 3. The following statements for CEG07b are also for CEG07a.

In Fig. 4, the DFM potentials in even ($ST = 01$ and 10) and odd ($ST = 00$ and 11) states are found to become less attractive and more repulsive, respectively, as E/A values become larger. Then, the attractive-to-repulsive transition is brought about by the sum of these four contributions. Although the energy dependence of the DFM potential comes partly

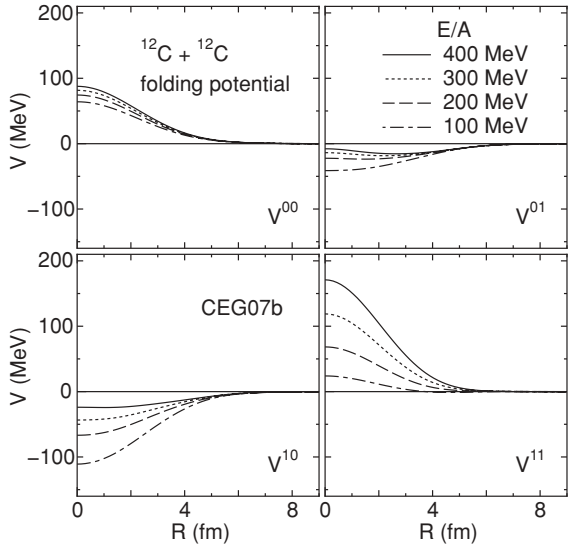

FIG. 4. Spin-isospin components ($S = 0$ or 1 and $T = 0$ or 1) of the real DFM potentials for the $^{12}C + ^{12}C$ elastic scattering at $E/A = 100$, 200, 300, and 400 MeV calculated with the CEG07b interaction. The dot-dashed, dashed, dotted, and solid curves are the results at $E/A = 100$, 200, 300, and 400 MeV, respectively.

from the folding procedure of the exchange part [Eq. (2)] and partly from the genuine energy dependence of the G-matrix interaction itself, the latter play a dominant role in our present problem. Basically, the energy dependence of the G-matrix interaction in the ST state can be imagined from the NN-scattering phase shifts in these states, by considering that our G-matrix represents a NN scattering in the nuclear medium: When scattering energies of NN pairs in the medium become higher with an increase of E/A, short-range repulsive parts of NN interactions make G matrices less attractive or more repulsive.

In Fig. 4, one notices that the V^{11} component has the largest energy dependence among the four components and plays a decisive role for the attractive-to-repulsive transition of the DFM potential. The difference among four components comes mainly from the two origins: One is the statistical factor $(2S + 1)(2T + 1)$ included in U^{ST}. This factor is the largest in the $S = T = 1$ state, which is the main reason for the largest contribution of V^{11} to the energy dependence of the DFM potential. The other is the tensor-force contribution. The energy dependence of V^{10} is stronger than that of V^{01}, although their $(2S + 1)(2T + 1)$ factors are equal to each other. The former includes the tensor force, but the latter does not, which is the main origin of the difference between the two cases. If the G matrix in the former is calculated with switching off the tensor force, its energy dependence becomes comparable to that for the latter. The tensor-force contribution is also important for the energy dependence of V^{11}.

Thus, it should be remarked that the existence of the attractive-to-repulsive transition is the critical prediction in our approach based on the realistic NN interactions, which include the tensor force, even if the transition energy is affected quantitatively by the unknown TBF contribution.

III. NEARSIDE AND FARSIDE DECOMPOSITIONS

The nearside and farside (N/F) decompositions of the differential cross sections are known to be very powerful tools for understanding the close relation between the attractive or the repulsive nature of optical potentials and the angular distribution of differential cross sections in the semiclassical manner [19]. In this section, we decompose the elastic-scattering cross sections calculated with the present DFM potentials into the N/F components to understand the characteristic behavior of the cross sections with the increase of the incident energy, shown in Fig. 2, and to clarify its close relation to the attractive-to-repulsive transition of the optical potentials, shown in Fig. 3, predicted by the present folding model.

We first depict the qualitative behavior of the incident particles (or the incident waves) under an attractive or a repulsive potential with a considerable absorption in the semiclassical picture. In the case in which there exists only a repulsive Coulomb potential between the projectile and the target nuclei in addition to an absorptive (imaginary) potential, all the incoming particles outside the grazing trajectories will, in the classical picture, be deflected to the scattering angles away from the target nucleus, which we define as the positive (or nearside) scattering angles. Now, let us define the scattering angle of the incident particle along the grazing trajectory as the grazing-scattering angle θ_{gr}. In the semiclassical picture, the scattering wave generated by such absorptive potential under the condition of the repulsive Coulomb field corresponds to the so-called edge wave generated at the nuclear surface along the grazing trajectory, the magnitude of which is shown to be symmetric around θ_{gr} in the semiclassical limit [19].

In the realistic cases of nucleus-nucleus scattering, there also exists a real part of the internucleus potential that is normally attractive ($V < 0$). In such cases, the incident particle along or inside the grazing trajectory can be deflected to the negative (farside) scattering angles if the attraction is strong enough. In the semiclassical picture, this corresponds to the situation in which the edge wave becomes asymmetric around θ_{gr} because the amplitude of the scattered wave on the target side is enhanced by the effect of the attractive potential. This causes the enhancement of the scattering into the negative (farside) angles that is compensated by the hindrance of the scattering to the positive (nearside) angles, which leads to a crossover between the nearside and farside amplitudes at a certain crossover angle, as shown in Fig. 5(a). In the crossover region, the two amplitudes have similar magnitudes that strongly interfere with each other, which show a typical Fraunhofer-type diffraction pattern in the angular distribution. At forward angles before the crossover region, the nearside amplitude dominates over the farside one, whereas the situation is reversed at backward angles. This is the typical situation widely seen in medium-energy scattering of light heavy-ion systems.

However, the situation will completely be changed if the nuclear potential is repulsive ($V > 0$), not attractive. In such a case, there exists no attraction that deflects the incident particle to the negative (farside) angles. Namely, in the semiclassical picture, the farside component of the scattered wave will be reduced by the repulsive nuclear potential while it enhances

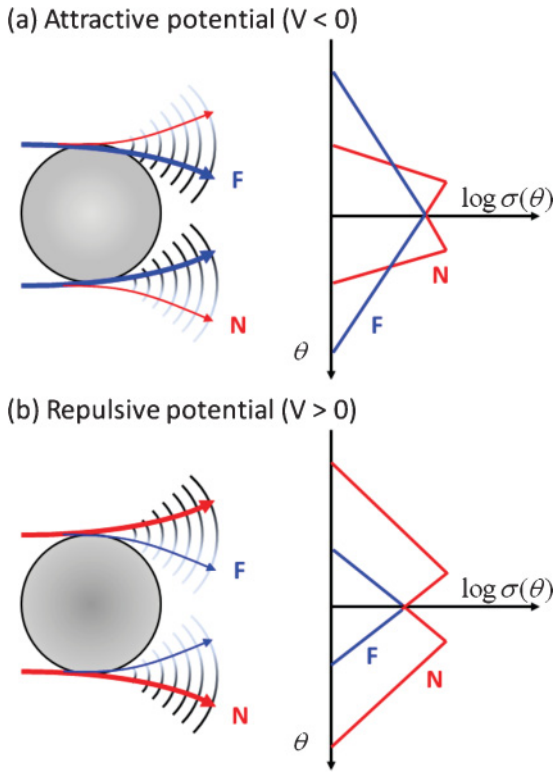

FIG. 5. (Color online) Schematics of the outgoing spherical waves and their amplitude strength (left) and semiclassical schematics of the N/F cross sections (right) in the cases of the (a) attractive and (b) repulsive potentials. The red and blue lines are the nearside and farside cross sections.

the nearside one and, hence, no crossover between the nearside and farside amplitudes occurs, as shown in Fig. 5(b).

Now, we have seen that the present folding model predicts the attractive-to-repulsive transition around the $E/A =$ 200–300 MeV region, the transition energy is dependent on the interaction used, and both the CEG07a and the CEG07b interactions give repulsive potentials ($V > 0$) at $E/A = 400$ MeV. Therefore, one may naturally expect that the effect of the drastic change of calculated real potentials with the increase of the incident energy should appear in the evolution of the calculated angular distribution of the elastic scattering. To understand the situation more quantitatively, we decompose the elastic-scattering cross sections into the N/F components in the quantum-mechanical way.

By following Ref. [19], the nuclear-scattering amplitude is decomposed into the N/F components by using the Legendre polynomials of the first kind $P_\ell(\cos\theta)$ and the second kind $Q_\ell(\cos\theta)$ as

$$f_N^{(\mathrm{Nucl.})}(\theta) = \sum (2\ell+1) a_\ell \tilde{Q}_\ell^{(-)}(\cos\theta), \tag{8}$$

$$f_F^{(\mathrm{Nucl.})}(\theta) = \sum (2\ell+1) a_\ell \tilde{Q}_\ell^{(+)}(\cos\theta), \tag{9}$$

where $\tilde{Q}_\ell^{(\pm)}(\cos\theta)$ are defined by

$$\tilde{Q}_\ell^{(\pm)}(\cos\theta) = \frac{1}{2}\left[P_\ell(\cos\theta) \mp i\frac{2}{\pi}Q_\ell(\cos\theta)\right]. \tag{10}$$

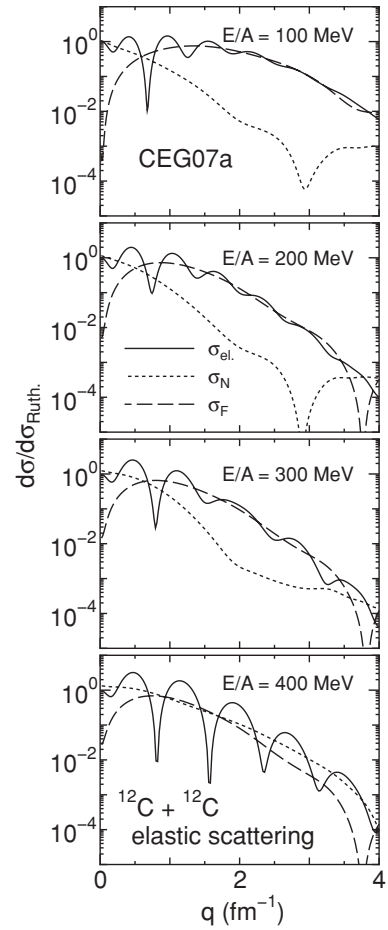

FIG. 6. Nearside and farside (N/F) decomposition of the elastic-scattering cross sections calculated from the CEG07a interaction with $N_W = 1.0$ for the $^{12}C + ^{12}C$ elastic scattering at $E/A =$ 100–400 MeV. The dotted, dashed, and solid curves are the N/F cross sections and the squared modules of their coherent sum, respectively.

The Rutherford amplitude is also decomposed into the nearside $f_N^{(\mathrm{Coul})}(\theta)$ and farside $f_F^{(\mathrm{Coul})}(\theta)$ components in the same manner as in Ref. [19]. Finally, the N/F cross sections are written as

$$\sigma_N = |f_N(\theta)|^2 = \left|f_N^{(\mathrm{Coul})}(\theta) + f_N^{(\mathrm{Nucl})}(\theta)\right|^2, \tag{11}$$

$$\sigma_F = |f_F(\theta)|^2 = \left|f_F^{(\mathrm{Coul})}(\theta) + f_F^{(\mathrm{Nucl})}(\theta)\right|^2, \tag{12}$$

and the full cross section is given by the squared modulus of their coherent sum,

$$\sigma_{\mathrm{el}} = |f_N(\theta) + f_F(\theta)|^2. \tag{13}$$

Figures 6 and 7 show the N/F cross sections together with the full cross sections calculated by DFM potentials with CEG07a and CEG07b at $E/A = 100$–400 MeV, respectively. At $E/A = 100$ MeV, the attraction of the real potential is very strong, as already seen in Fig. 3, which largely enhances the farside component and reduces the nearside one, and, hence, the farside component dominates over the nearside one at most scattering angles except for very forward angles. This is particularly clear in the case of the CEG07a interaction. The

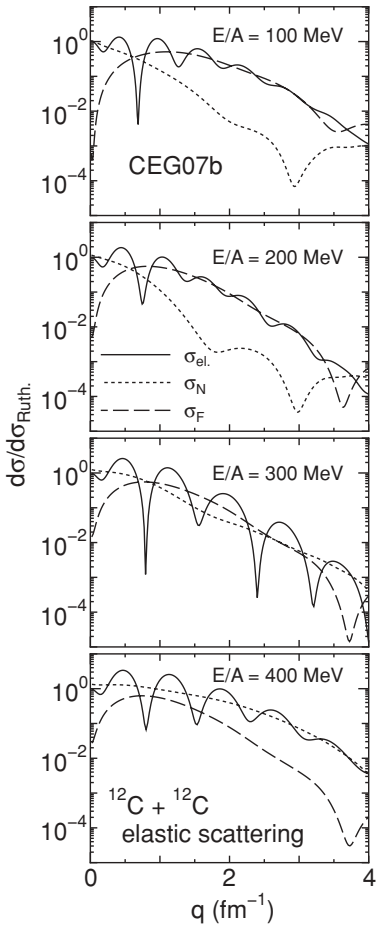

FIG. 7. Same as Fig. 6 but from the CEG07b interaction.

farside dominance persists up to $E/A = 300$ MeV in the case of the CEG07a interaction, while it does up to 200 MeV in the case of the CEG07b one. The difference comes, of course, from less attraction (see Fig. 3) in the case of the CEG07b interaction because of the repulsive TBF effect, as already discussed before.

At $E/A = 400$ MeV (300 MeV) in the case of the CEG07a (CEG07b) interaction, the nearside and farside components are seen to have comparable magnitudes and strongly interfere with each other by showing a strong N/F diffraction pattern in the angular distribution. The strong diffraction pattern implies that the contribution of the real potential becomes effectively minimum at the corresponding energy. In the case of the CEG07b interaction, one can clearly see the nearside dominance with the reduced N/F interference at $E/A = 400$ MeV, which is a clear signature generated by the repulsive nature of the real potential.

These results strongly suggest possible experimental evidence for the attractive-to-repulsive transition of the nucleus-nucleus optical potentials to be obtained by measuring the characteristic energy evolution of the elastic-scattering angular distribution in this energy region. Namely, the evidence would be obtained by observing the farside dominance at the lower energies and the nearside dominance at the higher energies both with less diffraction patterns caused by the reduced N/F interference, together with the strong diffraction around a certain transition energy in between caused by the strong N/F interference because of the comparable magnitudes of both components, although the predicted transition energy depends on the effective interaction used, which ranges from $E/A = 300$ to 400 MeV. The experimental determination of the transition energy will also provide us with more evidence for the repulsive TBF effect as well as information about the energy dependence of the repulsive TBF effect that has not yet been taken into account in the present folding model with the CEG07b interaction as already mentioned.

One may notice the attractive-to-repulsive transition energies estimated from the angular distributions (Figs. 6 and 7) are rather different from those seen in the calculated folding potentials (Fig. 3). As mentioned before, the calculated real potential starts to change its sign from negative (attractive) to positive (repulsive) around $E/A = 300$ MeV in the case of CEG07a and around $E/A = 200$ MeV in the case of CEG07b, while the transition energies estimated from the calculated cross sections are shifted to the higher-energy side by about 100 MeV. However, one should note the following point by comparing the potentials and cross sections. A close look at the calculated real potentials in the tail region for $E/A = 300$ MeV for CEG07a and 200 MeV for CEG07b makes one notice that the potentials are still slightly attractive in the tail region despite the strongly repulsive values in the short and middle radial ranges. Because of the existence of the absorptive potential, the contribution from the short-range part of the potential of a strongly repulsive nature should more or less be reduced by the absorption effect.

To see the effect of absorption on the elastic scattering more quantitatively, we plot the modulus of the S-matrix elements $|S_L|$ calculated with CEG07b in Fig. 8 as a function of the *effective radius* (or the so-called classical turning point) $R_{\rm cl}$ defined by $R_{\rm cl} = \sqrt{L(L+1)}/k \cong L/k$, where L and k are the orbital angular momentum (partial wave) and the wave number of the nucleus-nucleus relative motion. Despite the rather strong imaginary potentials, the S-matrix elements have considerable magnitudes for partial waves, which correspond to the radial range well inside the nuclear surface down to $R_{\rm cl} \approx 2$–2.5 fm, whereas they have negligible magnitudes for the $R_{\rm cl} < 2$-fm region. In fact, we have confirmed, with the notch test, that the scattering cross sections are quite sensitive to the potential in the radial range of $R > 3$ fm, while the potentials in the radial range of $R < 2$ fm are irrelevant to the cross sections over the angular range discussed in the present paper. This is quite consistent with the fact that the scattering cross sections at $E/A = 200$ MeV still show the characteristic property of attractive potential (Fig. 7) despite that the real potential at this energy is repulsive in the radial range of $R < 2.5$ fm, whereas the cross sections at $E/A = 300$ and 400 MeV reflect the repulsive nature of the potentials that have positive values in the radial range well outside 3 fm as shown in Fig. 3.

Figure 9 shows the same S-matrix elements $S_L = |S_L| \exp 2i\delta_L$ in the complex S plane. It is clearly seen that the phase shifts δ_L are positive for all L values in the cases of $E/A = 100$ and 200 MeV, whereas in the cases of $E/A = 300$ and 400 MeV, the phase shifts have negative sign for the partial

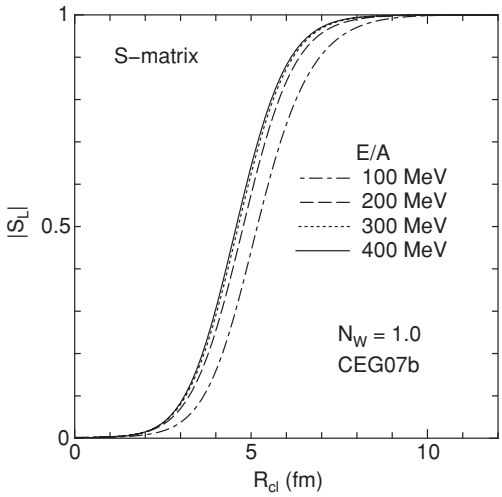

FIG. 8. The modulus of the S-matrix elements $|S_L|$ plotted as a function of the effective radius $R_{\rm cl} = L/k$ in the case of the CEG07b interaction.

waves $L < L_{\rm cr}$ where $L_{\rm cr}$ is the critical partial wave at which the phase shift changes its sign [$\delta_{L_{\rm cr}} \approx 0$ (i.e., Im $S_{L_{\rm cr}} \approx 0$)]. The negative sign of the phase shift ($\delta_L < 0$) implies that the potential is effectively repulsive for partial waves less than $L_{\rm cr}$. The effective radius $R_{\rm cr} = L_{\rm cr}/k$, which corresponds to the critical partial wave $L_{\rm cr}$ is about 3.5 fm for $E/A = 300$ MeV and 4.2 fm for $E/A = 400$ MeV, respectively, while the calculated potential itself changes its sign around $R = 4.1$ and 4.7 fm, respectively. This is naturally interpreted as (e.g., in the $E/A = 400$ MeV case) the effect of repulsion in the radial range of $4.2 < R < 4.7$ fm is canceled by the effect of attraction outside 4.7 fm, which leads to an almost-zero phase shift for the corresponding partial wave $L_{\rm cr}$. One should note that the $R_{\rm cr}$ values are large enough compared with the radius of complete absorption ($R \leqslant$ 2–2.5 fm) and, therefore, the elastic scattering at $E/A = 300$ and 400 MeV sufficiently probes the repulsive nature of the potential.

Thus, the existence of weak attraction in the low-density nuclear surface region, where the repulsive TBF effect is weak enough, together with the absorption well inside the nucleus ($R \leqslant$ 2.0–2.5 fm) will be the main origin of the fact we have just mentioned that the attractive-to-repulsive transition energy

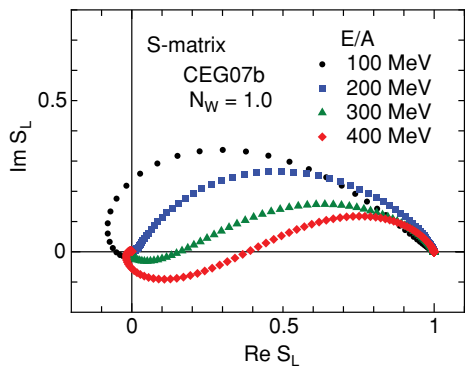

FIG. 9. (Color online) The S-matrix elements plotted in the complex S plane.

evaluated from the evolution of the scattering cross sections looks shifted to the higher-energy side with respect to what one naively expects from the calculated potentials themselves shown in Fig. 3. The amount of the energy shift may depend on the magnitude of the absorption effect, namely, on the adopted value of the renormalization factor N_W for the imaginary potential and, in Sec. IV, we examine how the conclusion depends on the adopted value of N_W.

IV. DISCUSSION ABOUT THEORETICAL AMBIGUITY

Now, let us discuss a possible range of ambiguity in the theoretical prediction for detecting the attractive-to-repulsive transition of the real potential through the observation of the angular distributions and their energy evolution.

The first source of ambiguity comes from the unknown energy dependence of the repulsive TBF contribution in the effective interaction. This was already discussed in this paper, and this is the reason why we have performed the calculation by using the two types of interactions, the CEG07a and CEG07b. The former contains no TBF effect, whereas the latter includes the TBF effect but neglects its energy dependence, which implies a possible overestimation of the TBF effect at highest energy. Hence, the truth may exist between the two extremes, although one cannot say in the present stage which is closer to the truth.

The second ambiguity of the present theoretical model is the renormalization factor N_W for the calculated imaginary potential. To see how the results we saw in Figs. 6 and 7 depend on the adopted value of N_W, we recalculate the cross section with different values of N_W in the case of CEG07b. Figure 10 shows the results with $N_W = 0.8$ and $N_W = 1.2$, instead of the original value $N_W = 1.0$ used in Fig. 7. By comparing the results of Fig. 10 with those of Fig. 7, one can see that the characteristic evolution of the calculated angular distribution with the increase in energy does not change at all qualitatively, except that the transition energy (at which the N/F cross sections become comparable) shifts by about 20 MeV to the lower-energy side for $N_W = 0.8$ and to the higher-energy side for $N_W = 1.2$ with respect to the original case of $N_W = 1.0$ shown in Fig. 7, although the detailed energy variations are not shown in the figures. The S-matrix elements calculated with $N_W = 0.8$ and 1.2 have quite similar behavior to what we saw in Figs. 8 and 9 with respect to the increasing energy. Therefore, we conclude that the ambiguity originated from the choice of the unknown strength of the imaginary-potential strength does not affect the conclusion drawn in Sec. III, except that the transition energy slightly changes (say, less than $\pm$20 MeV) with a rather drastic change of the N_W value by $\pm$20%. The experimental measurements of the energy evolution of the elastic scattering would rather give useful information about the N_W value to be used in addition to the real attractive-to-repulsive transition energy.

Another source of ambiguity to verify the attractive potential from the measured angular distribution will be related to the uniqueness of the potential that reproduces the experimental data. As is well known, it is often the case for heavy-ion scattering that one cannot determine the unique

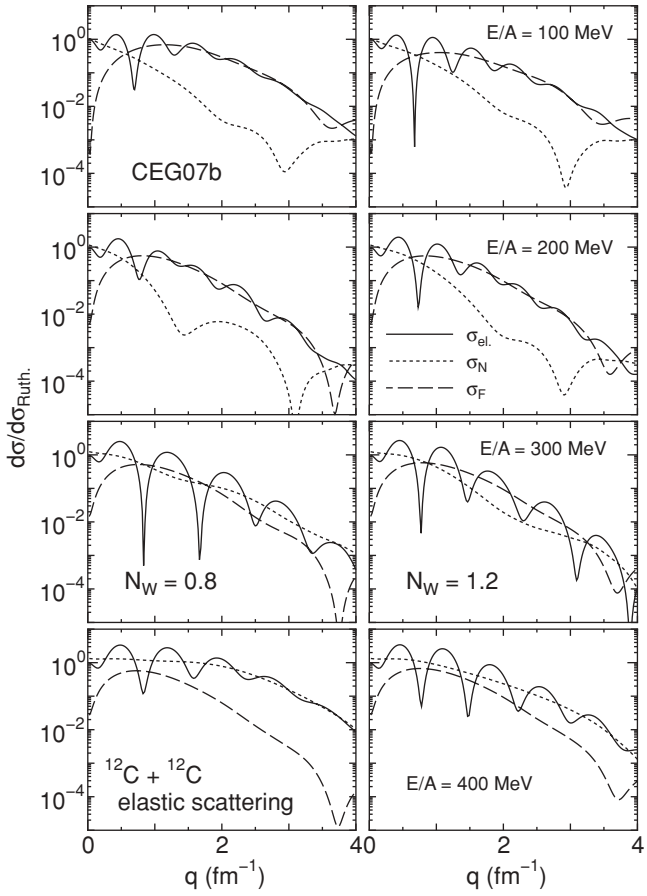

FIG. 10. Same as Fig. 7 but with $N_W = 0.8$ (left) and $N_W = 1.2$ (right).

optical potentials phenomenologically from the measured angular distribution of the elastic scattering due partly to the limited angular range of the measured angular distribution and partly to the existence of the strong absorption, which prevent us from probing the interior part of the real potential strengths and shapes.

To investigate the uniqueness of the calculated folding potential with respect to the measured cross sections, we have performed the following test calculation. Namely, we search for a model-independent phenomenological potential that reproduces the elastic-scattering cross sections calculated from the present DFM potential at $E/A = 400$ MeV that has the strongly repulsive real potential, by regarding the calculated cross sections as the virtual experimental data. In this analysis, we put a constraint upon the phenomenological potential that its real part is attractive rather than repulsive. Here, we have used an automatic potential search code ALPS [34] to search for the best-fit values of the parameters.

Figures 11 and 12 show the results. The filled dots in Fig. 11 are the cross sections calculated from the present DFM potential with the CEG07b interaction, that is, the same as those given in Fig. 2 or Fig. 7, although displayed as a function of the scattering angle θ rather than the momentum transfer q, whereas the dotted curve shows the result of the phenomenological optical potential so obtained that the potential reproduces the experimental cross sections calculated from

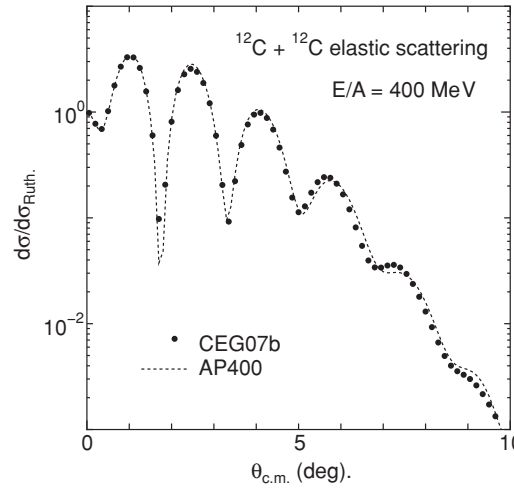

FIG. 11. Elastic-scattering cross sections calculated from the DFM potential with CEG07b and phenomenological potential (AP400) for the $^{12}C + ^{12}C$ system at $E/A = 400$ MeV. The filled dots and dotted curve are the results from the DFM potential with CEG07b and AP400, respectively.

the folding potential. We call the attractive phenomenological potential the AP400 potential. The dotted curves shown in Fig. 12 are the so-obtained AP400 potential, which has the attractive real part. The cross sections calculated from the AP400 potential can be very close to those obtained from the theoretical folding potential, which has the strongly repulsive real part as shown in Fig. 11. One might be

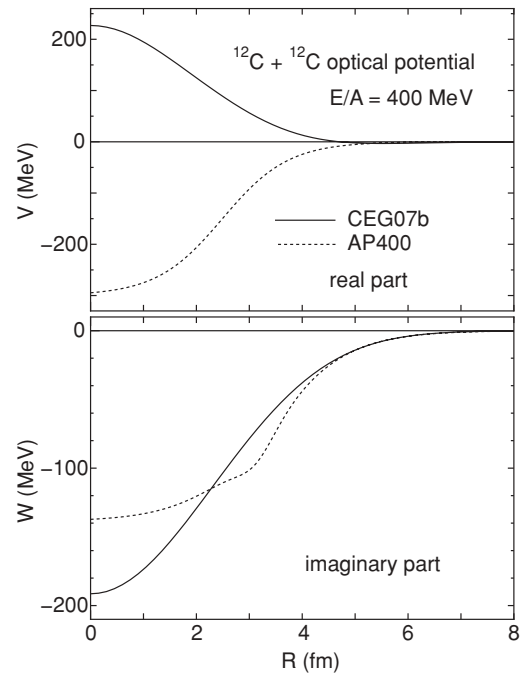

FIG. 12. Real (upper) and imaginary (lower) parts of the DFM potential with CEG07b and phenomenological potential (AP400) for the $^{12}C + ^{12}C$ elastic scattering at $E/A = 400$ MeV. The solid and dotted curves are the DFM potential with CEG07b and AP400, respectively.

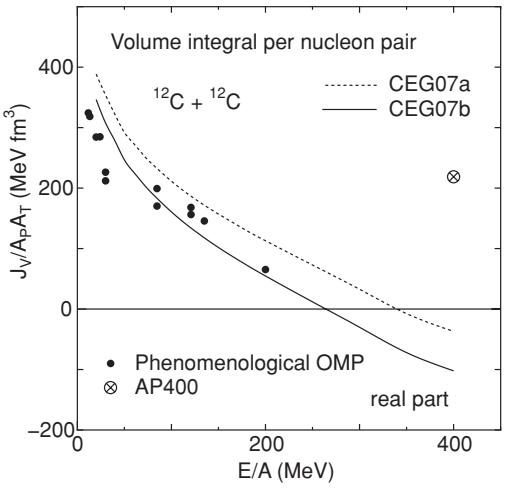

FIG. 13. Volume integrals per nucleon pair of the real part of the DFM potential with CEG07a and CEG07b, AP400, and phenomenological optical-model potential (OMP) for the $^{12}C + ^{12}C$ system. The solid circles are the results with the phenomenological OMP taken from Refs. [35–38]. The crossed circle is the result with AP400. The solid and dotted curves are the DFM potentials with CEG07b and CEG07a, respectively.

disappointed with this result that seems to force one to give up hope for obtaining evidence for the repulsiveness of the real potential.

However, the volume integral per nucleon pair, which is defined as positive for attractive ($V < 0$) potentials,

$$J_V/A_PA_P = -4\pi \int_0^\infty V(R)R^2\,dR/A_PA_P, \qquad (14)$$

of the real part of the AP400 potential so obtained has an extremely unrealistic value, as shown by the crossed circle in Fig. 13, which completely conflicts with the systematic energy dependence of J_V/A_PA_P extracted from the optical potentials in the lower-energy region. On the other hand, the J_V/A_PA_P values predicted by the present folding model are consistent with the systematics, and their values change from attractive ($J_V/A_PA_P > 0$) to repulsive ($J_V/A_PA_P < 0$) around $E/A \approx$ 300 MeV. This result preserves our hope to get clear evidence of the repulsive nature of nucleus-nucleus optical potentials by measuring the elastic-scattering angular distributions in this energy range.

V. SUMMARY AND CONCLUSION

The real part of heavy-ion optical potentials is believed to be attractive in the low-energy region at least less than $E/A \approx$ 200 MeV where experimental data for the elastic scattering exist. However, the potentials are predicted to change their character from attractive to repulsive around the energies of $E/A \approx$ 200–300 MeV and to become strongly repulsive above $E/A \approx$ 400 MeV by the microscopic DFM based on the complex G-matrix interaction CEG07 [16–18]. In this paper, we have shown that the tensor force plays an important role for lowering the attractive-to-repulsive transition energy of the DFM potentials by decomposing the potentials into the spin-isospin components. It is also shown that the nearside and farside (N/F) decompositions of the elastic-scattering cross sections clarify the close relation between the attractive-to-repulsive transition of the calculated DFM potentials and the characteristic evolution of the elastic-scattering angular distributions with the increase of the incident energy in the range of $E/A =$ 100–400 MeV.

No experimental evidence exists so far for the repulsive nature of heavy-ion optical potentials in this energy range because of the lack of experimental data above $E/A =$ 200 MeV. Therefore, on the basis of the present analyses, here, we propose the experimental measurements of elastic-scattering angular distributions in the $^{12}C + ^{12}C$ system, particularly the careful measurements of the characteristic evolution of the diffraction pattern with the increase of the incident energy in the range of $E/A =$ 200–400 MeV. More explicitly, we propose the observation of a strong diffraction pattern caused by the interference between the nearside and the farside amplitudes, both having comparable magnitudes, around the attractive-to-repulsive transition energy, together with the observation of less diffractive patterns in the farside-dominant regime (i.e., the attractive-potential regime) on the lower-energy side as well as in the nearside-dominant regime (the repulsive-potential regime) on the higher-energy side that we have seen in Figs. 6–10. Such experiments will provide us with decisive evidence for the repulsive nature of heavy-ion optical potentials as well as information about the energy region where the attractive-to-repulsive transition occurs.

The theoretical ambiguity caused by the unknown strength of the predicted imaginary potential is found to give only a minor effect on the determination of the attractive-to-repulsive transition energy. On the other hand, the transition energy strongly depends on the interaction models used, namely, CEG07b with the TBF effect and the CEG07a without the effect. Therefore, the experimental determination of the transition energy through the precise measurement of elastic scattering provides quite important information about the TBF effect (particularly, its repulsive component), which is one of the most important medium effects in high-density nuclear matter, and its energy dependence, in addition to the role of the tensor force that is one of the main origins of the energy dependence of the heavy-ion optical potentials in the present energy region.

ACKNOWLEDGMENTS

The authors thank Professor Th. A. Rijken for valuable comments and discussions about the NN potential. The authors thank Professor Y. Iseri for allowing them to use the ALPS computer code for the optimum potential research performed in this paper. The authors thank Dr. M. Takashina for useful advice and valuable comments.

APPENDIX

In this appendix, we give the parameters of CEG07a and CEG07b interactions fitted as a function of ρ to use in the DFM calculation. The CEG07 interactions have Gaussian

TABLE I. Parameters $v_{ik}^{ST}(E/A)$ of Eq. (A1) for real and imaginary components of CEG07a at $E/A = 200$ MeV.

		Real part						Imaginary part			
k	i	$S=0, T=0$	$S=0, T=1$	$S=1, T=0$	$S=1, T=1$	k	i	$S=0, T=0$	$S=0, T=1$	$S=1, T=0$	$S=1, T=1$
	1	1.4984×10^{2}	5.1631×10^{2}	6.7703×10^{2}	-5.5283×10^{2}		1	-5.4938×10^{1}	1.9255×10^{2}	3.1513×10^{2}	-2.7959×10^{2}
1	2	5.8796×10^{2}	1.0180×10^{3}	2.5437×10^{3}	1.4024×10^{3}	1	2	1.5391×10^{2}	-6.8343×10^{2}	5.0538×10^{2}	1.1973×10^{3}
	3	-7.1838×10^{2}	-3.1219×10^{3}	-9.5855×10^{3}	-2.4000×10^{3}		3	-1.1832×10^{3}	1.1808×10^{3}	-4.5675×10^{3}	-3.8936×10^{3}
	4	7.7232×10^{2}	3.6918×10^{3}	1.0844×10^{4}	1.9947×10^{3}		4	1.8930×10^{3}	-8.9920×10^{2}	6.1633×10^{3}	4.7417×10^{3}
	1	1.4027×10^{2}	-1.6210×10^{2}	-1.8304×10^{2}	1.8181×10^{1}		1	-6.3098×10^{1}	-6.2333×10^{1}	-1.6207×10^{2}	-3.5977×10^{1}
2	2	3.0356×10^{2}	-1.6429×10^{2}	-9.2344×10^{2}	1.2040×10^{2}	2	2	1.9972×10^{2}	2.3987×10^{2}	1.0764×10^{2}	1.3253×10^{2}
	3	-6.5446×10^{2}	8.3012×10^{2}	3.4647×10^{3}	-2.4214×10^{2}		3	-6.3899×10^{2}	-4.9286×10^{2}	8.6173×10^{2}	-4.0087×10^{2}
	4	5.5452×10^{2}	-1.0512×10^{3}	-3.7746×10^{3}	1.8618×10^{2}		4	8.3661×10^{2}	4.2019×10^{2}	-1.4043×10^{3}	4.9445×10^{2}
	1	7.4441×10^{0}	-4.2227×10^{0}	-5.1531×10^{0}	4.9278×10^{-1}		1	-5.6490×10^{-1}	-2.1836×10^{-1}	-1.3051×10^{0}	-8.4595×10^{-2}
3	2	3.3146×10^{-1}	3.3261×10^{0}	1.5867×10^{1}	-9.5806×10^{-1}	3	2	-5.5276×10^{0}	4.4644×10^{-2}	1.0811×10^{1}	-1.7028×10^{0}
	3	8.8642×10^{-2}	-1.2133×10^{1}	-5.1867×10^{1}	2.4155×10^{0}		3	2.8273×10^{1}	-1.6156×10^{-1}	-2.6601×10^{1}	8.0044×10^{0}
	4	-2.8656×10^{-1}	1.4728×10^{1}	5.4100×10^{1}	-2.3407×10^{0}		4	-3.6347×10^{1}	1.2218×10^{0}	2.0526×10^{1}	-1.0264×10^{1}

TABLE II. Parameters $v_{ik}^{ST}(E/A)$ of Eq. (A1) for real and imaginary components of CEG07a at $E/A = 300$ MeV.

		Real part						Imaginary part			
k	i	$S=0, T=0$	$S=0, T=1$	$S=1, T=0$	$S=1, T=1$	k	i	$S=0, T=0$	$S=0, T=1$	$S=1, T=0$	$S=1, T=1$
	1	6.9056×10^{1}	7.1604×10^{2}	9.8365×10^{2}	-3.0975×10^{2}		1	-1.2479×10^{0}	1.8246×10^{2}	3.7571×10^{2}	-2.3442×10^{2}
1	2	7.6353×10^{2}	-9.2643×10^{2}	-1.0961×10^{3}	6.3585×10^{2}	1	2	-1.5231×10^{2}	-8.7240×10^{2}	-1.1738×10^{3}	6.0893×10^{2}
	3	-1.0748×10^{3}	4.4202×10^{3}	4.0427×10^{3}	-4.2966×10^{2}		3	-4.4962×10^{2}	1.9740×10^{3}	2.5215×10^{3}	-1.7180×10^{3}
	4	1.2152×10^{3}	-5.6635×10^{3}	-5.4054×10^{3}	-3.1103×10^{0}		4	1.1106×10^{3}	-1.9388×10^{3}	-2.4696×10^{3}	2.0026×10^{3}
	1	1.6768×10^{2}	-2.1820×10^{2}	-2.8127×10^{2}	4.0169×10^{1}		1	-8.6144×10^{1}	-5.8552×10^{1}	-1.8790×10^{2}	-4.2335×10^{1}
2	2	1.7540×10^{2}	5.5531×10^{2}	4.6296×10^{2}	1.7067×10^{1}	2	2	1.6236×10^{2}	2.6777×10^{2}	6.7495×10^{2}	9.3420×10^{1}
	3	-2.3012×10^{2}	-1.9468×10^{3}	-1.6558×10^{3}	5.9443×10^{1}		3	-2.3973×10^{2}	-6.6465×10^{2}	-1.4602×10^{3}	-1.7294×10^{2}
	4	4.0496×10^{1}	2.3658×10^{3}	2.2388×10^{3}	-1.5041×10^{2}		4	2.3685×10^{2}	6.7796×10^{2}	1.3777×10^{3}	1.7996×10^{2}
	1	7.4520×10^{0}	-3.6216×10^{0}	-2.6577×10^{0}	1.9374×10^{-1}		1	-1.0053×10^{0}	-1.4320×10^{-1}	-1.2462×10^{-1}	-2.0072×10^{-1}
3	2	7.8453×10^{-1}	-8.5965×10^{0}	-1.0904×10^{1}	-1.2268×10^{-1}	3	2	5.7446×10^{0}	-1.5753×10^{0}	-1.2981×10^{-1}	1.6593×10^{0}
	3	-1.3172×10^{0}	3.6005×10^{1}	4.6389×10^{1}	7.0192×10^{-1}		3	-2.3322×10^{1}	4.9829×10^{0}	-2.9679×10^{0}	-6.6956×10^{0}
	4	1.5322×10^{0}	-4.5563×10^{1}	-6.4246×10^{1}	-5.0809×10^{-1}		4	2.9606×10^{1}	-4.6909×10^{0}	7.3243×10^{0}	8.1417×10^{0}

TABLE III. Parameters $v_{ik}^{ST}(E/A)$ of Eq. (A1) for real and imaginary components of CEG07a at $E/A = 400$ MeV.

		Real part						Imaginary part			
k	i	$S=0, T=0$	$S=0, T=1$	$S=1, T=0$	$S=1, T=1$	k	i	$S=0, T=0$	$S=0, T=1$	$S=1, T=0$	$S=1, T=1$
	1	-9.7829×10^{1}	7.5075×10^{2}	9.2119×10^{2}	-1.8643×10^{2}		1	7.2634×10^{1}	1.5607×10^{2}	1.8831×10^{2}	-1.8681×10^{2}
1	2	1.5595×10^{3}	-1.8542×10^{3}	-4.3896×10^{3}	6.8908×10^{2}	1	2	-2.3638×10^{2}	-1.0909×10^{3}	-2.5060×10^{3}	2.3976×10^{2}
	3	-3.2607×10^{3}	1.0933×10^{4}	2.3070×10^{4}	-1.0680×10^{3}		3	-1.0166×10^{3}	2.8250×10^{3}	1.2772×10^{4}	-6.8849×10^{2}
	4	3.5865×10^{3}	-1.5834×10^{4}	-3.2444×10^{4}	9.6152×10^{2}		4	2.2188×10^{3}	-2.9880×10^{3}	-1.8106×10^{4}	9.1688×10^{2}
	1	2.1474×10^{2}	-2.1535×10^{2}	-2.5301×10^{2}	6.4136×10^{1}		1	-1.1953×10^{2}	-5.3156×10^{1}	-1.3096×10^{2}	-5.1386×10^{1}
2	2	-5.1670×10^{1}	9.5194×10^{2}	1.8300×10^{3}	-7.7905×10^{1}	2	2	2.0318×10^{2}	3.0960×10^{2}	1.2299×10^{3}	8.4118×10^{1}
	3	4.0749×10^{2}	-4.5903×10^{3}	-9.2040×10^{3}	2.8059×10^{2}		3	-4.6583×10^{1}	-8.4612×10^{2}	-5.4605×10^{3}	-4.3759×10^{1}
	4	-6.4672×10^{2}	6.4186×10^{3}	1.2801×10^{4}	-3.6296×10^{2}		4	-1.8726×10^{2}	9.1945×10^{2}	7.4257×10^{3}	-2.5925×10^{1}
	1	7.3826×10^{0}	-3.3189×10^{0}	-1.9923×10^{0}	-3.1741×10^{-1}		1	-6.5069×10^{-1}	-2.9304×10^{-1}	-3.3762×10^{-1}	-5.4267×10^{-2}
3	2	2.4851×10^{0}	-2.2008×10^{1}	-4.8395×10^{1}	1.9791×10^{0}	3	2	7.5150×10^{0}	-2.0457×10^{0}	-2.0652×10^{1}	1.8346×10^{0}
	3	-6.7304×10^{0}	1.1153×10^{2}	2.4044×10^{2}	-4.5758×10^{0}		3	-3.8504×10^{1}	6.2414×10^{0}	1.1352×10^{2}	-9.6070×10^{0}
	4	7.7198×10^{0}	-1.5678×10^{2}	-3.3358×10^{2}	5.1343×10^{0}		4	5.3296×10^{1}	-6.2061×10^{0}	-1.6174×10^{2}	1.3079×10^{1}

TABLE IV. Parameters $v_{ik}^{ST}(E/A)$ of Eq. (A1) for real and imaginary components of CEG07b at $E/A = 200$ MeV.

		Real part						Imaginary part			
k	i	$S=0, T=0$	$S=0, T=1$	$S=1, T=0$	$S=1, T=1$	k	i	$S=0, T=0$	$S=0, T=1$	$S=1, T=0$	$S=1, T=1$
	1	1.5026×10^{2}	5.1753×10^{2}	6.7321×10^{2}	-5.5239×10^{2}		1	-5.5932×10^{1}	1.9416×10^{2}	3.1525×10^{2}	-2.7928×10^{2}
1	2	1.0226×10^{3}	1.1364×10^{3}	3.3032×10^{3}	1.6156×10^{3}	1	2	4.0234×10^{1}	-9.2867×10^{2}	4.5322×10^{2}	1.4623×10^{3}
	3	-6.3548×10^{2}	-4.4520×10^{3}	-9.9580×10^{3}	-3.5164×10^{3}		3	-1.1107×10^{3}	1.4589×10^{3}	-3.9580×10^{3}	-4.4331×10^{3}
	4	2.6396×10^{3}	5.3540×10^{3}	9.5866×10^{3}	3.1849×10^{3}		4	2.1241×10^{3}	-7.4432×10^{2}	4.8241×10^{3}	5.2155×10^{3}
	1	1.4015×10^{2}	-1.6276×10^{2}	-1.8230×10^{2}	1.8059×10^{1}		1	-6.3593×10^{1}	-6.2758×10^{1}	-1.6254×10^{2}	-3.6103×10^{1}
2	2	3.3278×10^{2}	-1.3203×10^{2}	-1.0752×10^{3}	1.9412×10^{2}	2	2	1.9582×10^{2}	3.3910×10^{2}	1.0865×10^{2}	1.1522×10^{2}
	3	-5.0928×10^{2}	1.2450×10^{3}	3.2687×10^{3}	-1.1961×10^{2}		3	-5.5544×10^{2}	-7.0030×10^{2}	8.7851×10^{2}	-3.6738×10^{2}
	4	3.9873×10^{2}	-1.6345×10^{3}	-3.1120×10^{3}	8.6328×10^{1}		4	7.2806×10^{2}	5.2501×10^{2}	-1.3040×10^{3}	4.9612×10^{2}
	1	7.4431×10^{0}	-4.2128×10^{0}	-5.1624×10^{0}	4.9272×10^{-1}		1	-5.3358×10^{-1}	-2.1665×10^{-1}	-1.2905×10^{0}	-7.7062×10^{-2}
3	2	7.8720×10^{-1}	4.9120×10^{0}	1.7612×10^{1}	-8.3881×10^{-1}	3	2	-7.8966×10^{0}	-1.4138×10^{0}	3.3460×10^{0}	-1.8603×10^{0}
	3	8.9499×10^{-1}	-1.6663×10^{1}	-5.1734×10^{1}	2.8412×10^{0}		3	2.5303×10^{1}	5.1614×10^{0}	1.0682×10^{0}	5.6959×10^{0}
	4	-1.7859×10^{0}	2.2032×10^{1}	5.0505×10^{1}	-2.8473×10^{0}		4	-2.2791×10^{1}	-2.7216×10^{0}	-1.1294×10^{1}	-5.5278×10^{0}

TABLE V. Parameters $v_{ik}^{ST}(E/A)$ of Eq. (A1) for real and imaginary components of CEG07b at $E/A = 300$ MeV.

		Real part						Imaginary part			
k	i	$S=0,T=0$	$S=0,T=1$	$S=1,T=0$	$S=1,T=1$	k	i	$S=0,T=0$	$S=0,T=1$	$S=1,T=0$	$S=1,T=1$
	1	6.8558×10^{1}	7.1731×10^{2}	9.8497×10^{2}	-3.1041×10^{2}		1	-2.2773×10^{0}	1.8413×10^{2}	3.7509×10^{2}	-2.3378×10^{2}
1	2	8.6525×10^{2}	-8.2674×10^{2}	-4.2141×10^{2}	7.4470×10^{2}	1	2	-1.8678×10^{2}	-1.1264×10^{3}	-1.4441×10^{3}	9.9280×10^{2}
	3	-7.1700×10^{2}	3.3033×10^{3}	4.2401×10^{3}	-1.1196×10^{3}		3	-1.0853×10^{3}	2.2942×10^{3}	3.8738×10^{3}	-2.7019×10^{3}
	4	2.2949×10^{3}	-4.5154×10^{3}	-7.2640×10^{3}	5.3886×10^{2}		4	2.2863×10^{3}	-1.7767×10^{3}	-4.0887×10^{3}	2.9501×10^{3}
	1	1.6782×10^{2}	-2.1881×10^{2}	-2.8222×10^{2}	4.0117×10^{1}		1	-8.5944×10^{1}	-5.9022×10^{1}	-1.8802×10^{2}	-4.2368×10^{1}
2	2	2.0451×10^{2}	6.0016×10^{2}	3.2762×10^{2}	9.0072×10^{1}	2	2	1.3722×10^{2}	3.6109×10^{2}	7.2945×10^{2}	6.3077×10^{1}
	3	-9.2524×10^{1}	-1.6289×10^{3}	-1.9090×10^{3}	1.9151×10^{2}		3	-8.3230×10^{1}	-8.5347×10^{2}	-1.5791×10^{3}	-1.1509×10^{2}
	4	-8.3180×10^{1}	1.9685×10^{3}	2.8760×10^{3}	-2.5771×10^{2}		4	7.3650×10^{1}	7.4775×10^{2}	1.4391×10^{3}	1.6703×10^{2}
	1	7.4512×10^{0}	-3.6021×10^{0}	-2.6175×10^{0}	1.9381×10^{-1}		1	-1.0319×10^{0}	-1.3113×10^{-1}	-1.1878×10^{-1}	-2.0691×10^{-1}
3	2	1.7328×10^{0}	-6.8656×10^{0}	-8.7448×10^{0}	6.8246×10^{-2}	3	2	4.6425×10^{0}	-3.0767×10^{0}	-8.0300×10^{0}	1.7655×10^{0}
	3	-1.5750×10^{0}	3.0447×10^{1}	4.7628×10^{1}	1.6016×10^{0}		3	-2.9188×10^{1}	9.6226×10^{0}	1.4997×10^{1}	-8.0323×10^{0}
	4	5.3477×10^{-1}	-3.6960×10^{1}	-7.1589×10^{1}	-2.0360×10^{0}		4	3.9976×10^{1}	-6.7011×10^{0}	-7.9961×10^{-1}	8.9123×10^{0}

TABLE VI. Parameters $v_{ik}^{ST}(E/A)$ of Eq. (A1) for real and imaginary components of CEG07b at $E/A = 400$ MeV.

		Real part						Imaginary part			
k	i	$S=0,T=0$	$S=0,T=1$	$S=1,T=0$	$S=1,T=1$	k	i	$S=0,T=0$	$S=0,T=1$	$S=1,T=0$	$S=1,T=1$
	1	-9.9111×10^{1}	7.4925×10^{2}	9.2599×10^{2}	-1.8744×10^{2}		1	7.0837×10^{1}	1.5706×10^{2}	1.8150×10^{2}	-1.8655×10^{2}
1	2	1.5540×10^{3}	-1.5565×10^{3}	-4.0825×10^{3}	6.8628×10^{2}	1	2	-2.1009×10^{2}	-1.2819×10^{3}	-2.4435×10^{3}	6.7759×10^{2}
	3	-2.8480×10^{3}	9.0725×10^{3}	2.5227×10^{4}	-1.2598×10^{3}		3	-1.8395×10^{3}	2.8845×10^{3}	1.3262×10^{4}	-1.7194×10^{3}
	4	4.1291×10^{3}	-1.4214×10^{4}	-3.6528×10^{4}	8.1700×10^{2}		4	3.2336×10^{3}	-2.3919×10^{3}	-1.9208×10^{4}	1.7672×10^{3}
	1	2.1513×10^{2}	-2.1488×10^{2}	-2.5526×10^{2}	6.4258×10^{1}		1	-1.1924×10^{2}	-5.3306×10^{1}	-1.2869×10^{2}	-5.1489×10^{1}
2	2	-2.0782×10^{1}	9.3134×10^{2}	1.8153×10^{3}	-3.4511×10^{0}	2	2	1.6864×10^{2}	3.6930×10^{2}	1.1430×10^{3}	3.6205×10^{1}
	3	5.0868×10^{2}	-4.0296×10^{3}	-1.0100×10^{4}	4.0204×10^{2}		3	1.0231×10^{2}	-8.9970×10^{2}	-5.1976×10^{3}	7.0411×10^{1}
	4	-6.9155×10^{2}	5.8769×10^{3}	1.4181×10^{4}	-4.4168×10^{2}		4	-2.8408×10^{2}	7.9363×10^{2}	7.2666×10^{3}	-1.0750×10^{2}
	1	7.3728×10^{0}	-3.3247×10^{0}	-1.9313×10^{0}	-3.2232×10^{-1}		1	-6.7917×10^{-1}	-2.9157×10^{-1}	-3.9885×10^{-1}	-5.9758×10^{-2}
3	2	4.3890×10^{0}	-1.8609×10^{1}	-4.7479×10^{1}	2.5728×10^{0}	3	2	6.0749×10^{0}	-2.2576×10^{0}	-2.3041×10^{1}	2.1387×10^{0}
	3	-1.0033×10^{1}	9.8089×10^{1}	2.5400×10^{2}	-5.4484×10^{0}		3	-3.8920×10^{1}	4.6533×10^{0}	1.0629×10^{2}	-1.0702×10^{1}
	4	9.7371×10^{0}	-1.4065×10^{2}	-3.5873×10^{2}	6.1425×10^{0}		4	5.1702×10^{1}	5.8632×10^{-1}	-1.4252×10^{2}	1.2891×10^{1}

form factor, and the parameters were fixed as

$$v^{ST}(s,\rho,E/A)=\sum_{k=1}^{3}\sum_{i=1}^{4}v_{ik}^{ST}(E/A)\rho^{i-1}\exp\left(-\frac{s^2}{\lambda_k^2}\right), \tag{A1}$$

in terms of v^{ST}, the spin-isospin component ($S=0$ or 1 and $T=0$ or 1) of the G-matrix interaction. Here, λ_1, λ_2, and λ_3 are fixed to be 0.5, 0.9, and 2.5, respectively. The parameters $v_{ik}^{ST}(E/A)$ for CEG07a at $E/A=200$, 300, and 400 MeV are given in Tables I–III and for CEG07b in Tables IV–VI. Here, we note that these parameters are fitted up to $k_F=1.8$ fm^{-1} ($\rho\approx 0.39$ fm^{-3}).

[1] C. Mahaux and R. Sartor, Adv. Nucl. Phys. **20**, 1 (1991).
[2] A. Nadasen, P. Schwandt, P. P. Singh, W. W. Jacobs, A. D. Bacher, P. T. Debevec, M. D. Kaitchuck, and J. T. Meek, Phys. Rev. C **23**, 1023 (1981).
[3] L. G. Arnold, B. C. Clark, and R. L. Mercer, Phys. Rev. C **19**, 917 (1979).
[4] L. G. Arnold *et al.*, Phys. Rev. C **25**, 936 (1982).
[5] L. Rikus, K. Nakano, and H. V. V. Geramb, Nucl. Phys. A **414**, 413 (1984).
[6] L. Rikus and H. V. V. Geramb, Nucl. Phys. A **426**, 496 (1984).
[7] S. Hama, B. C. Clark, E. D. Cooper, H. S. Sherif, and R. L. Mercer, Phys. Rev. C **41**, 2737 (1990).
[8] E. D. Cooper, S. Hama, B. C. Clark, and R. L. Mercer, Phys. Rev. C **47**, 297 (1993).
[9] N. V. Sen *et al.*, Phys. Lett. B **156**, 185 (1985).
[10] N. V. Sen *et al.*, Nucl. Phys. A **464**, 717 (1987).
[11] J. S. Al Khalili, J. A. Tostevin, and R. C. Johnson, Phys. Rev. C **41**, R806 (1990).
[12] V. K. Mishra, S. Hama, B. C. Clark, R. E. Kozack, R. L. Mercer, and L. Ray, Phys. Rev. C **43**, 801 (1991).
[13] Y. Sakuragi and M. Tanifuji, Nucl. Phys. A **560**, 945 (1993).
[14] M. Nakano, H. Matsuura, T. Maki, M. Matoba, and H. Ohgaki, Phys. Rev. C **40**, 1323 (1989).
[15] T. Furumoto, Y. Sakuragi, and Y. Yamamoto, Phys. Rev. C **78**, 044610 (2008).
[16] T. Furumoto, Y. Sakuragi, and Y. Yamamoto, Phys. Rev. C **79**, 011601(R) (2009).
[17] T. Furumoto, Y. Sakuragi, and Y. Yamamoto, Phys. Rev. C **80**, 044614 (2009).
[18] T. Furumoto, Y. Sakuragi, and Y. Yamamoto, Phys. Rev. C **82**, 029908(E) (2010).
[19] R. C. Fuller, Phys. Rev. C **12**, 1561 (1975).
[20] T. A. Rijken, Phys. Rev. C **73**, 044007 (2006).
[21] T. A. Rijken and Y. Yamamoto, Phys. Rev. C **73**, 044008 (2006).
[22] B. Sinha, Phys. Rep. **20**, 1 (1975).
[23] B. Sinha and S. A. Moszkowski, Phys. Lett. B **81**, 289 (1979).
[24] J. W. Negele and D. M. Vautherin, Phys. Rev. C **5**, 1472 (1972).
[25] X. Campi and A. Bouyssy, Phys. Lett. B **73**, 263 (1978).
[26] D. T. Khoa, Phys. Rev. C **63**, 034007 (2001).
[27] S. Nagata, M. Kamimura, and N. Yamaguchi, Prog. Theor. Phys. **73**, 512 (1985).
[28] D. T. Khoa, W. von Oertzen, and H. G. Bohlen, Phys. Rev. C **49**, 1652 (1994).
[29] D. T. Khoa, G. R. Satchler, and W. von Oertzen, Phys. Rev. C **56**, 954 (1997).
[30] M. Katsuma, Y. Sakuragi, S. Okabe, and Y. Kondo, Prog. Theor. Phys. **107**, 377 (2002).
[31] G. R. Satchler and W. G. Love, Phys. Rep. **55**, 184 (1979).
[32] H. DeVries, C. W. DeJager, and C. DeVries, At. Data Nucl. Data Tables **36**, 495 (1987).
[33] L. R. B. Elton, *Nuclear Sizes* (Oxford University Press, Oxford, 1961).
[34] Y. Iseri, computer code ALPS (unpublished).
[35] M. Buenerd, A. Lounis, J. Chauvin, D. Lebrun, P. Martin, G. Duhamel, J. C. Gondrand, and P. D. Saintignon, Nucl. Phys. A **424**, 313 (1984).
[36] M. E. Brandan and G. R. Satchler, Nucl. Phys. A **487**, 477 (1988).
[37] J. Y. Hostachy *et al.*, Nucl. Phys. A **490**, 441 (1988).
[38] T. Ichihara *et al.*, Phys. Lett. B **323**, 278 (1994).